RSC Advances

RSC Advances

www.rsc.org/advances

ROYAL SOCIETY OF CHEMISTRY

www.rsc.org/advances

RSC Advances

ARTICLE

$CoFe_2O_4$ and $NiFe_2O_4$ @ graphene adsorbents for heavy metal ions – Kinetic and Thermodynamic analysis

Chella Santhosh,[a] Pratap Kollu, [b] Sathiyanathan Felix,[a] Soon Kwan Jeong[*c] and Andrews Nirmala Grace[*a,c]

Magnetic cobalt and nickel ferrites ($CoFe_2O_4$ & $NiFe_2O_4$) with graphene nanocomposites ($CoFe_2O_4$-G & $NiFe_2O_4$-G) were synthesized via solvothermal process and used as an adsorbent for removal of lead (Pb(II)) and cadmium (Cd(II)) ions from aqueous solution. The as-prepared materials were characterized by field emission- scanning electron microscope (FE-SEM), X-ray diffraction (XRD), Brunauer–Emmett–Teller (BET) surface area analyzer, transmission electron microscope (TEM) and VSM analysis. To probe the nature of the adsorbent, various experiments were investigated like contact time, adsorbent dose, solution pH and temperature were optimized. The isotherm model fitting studies demonstrated that the data fitted well to Langmuir isotherm model. The highest adsorption equilibrium for Pb(II) is 142.8 and 111.1 mg/g at pH of 5 and 310 K for $CoFe_2O_4$-G & $NiFe_2O_4$-G; while for Cd(II) was 105.26 and 74.62 mg/g at pH of 7 and 310 K. Results show that such type of materials could be used for the removal of heavy metal ions from water for environmental applications.

INTRODUCTION

Due to globalization, rapid developments in industrialization, urbanization and population have largely contributed to the severe pollution of water, air and soil. Among these, drinking safe water has become the major concern for practical utility. Major industries are producing wastewater that contains harmful toxic metal ions. Heavy metal ions are one of the major harmful contaminants in water[1–3] and to counteract it, various processes like chemical, physical and biological have been developed to prevent the pollution successfully[4-9]. Among these processes, adsorption is one of the widely used process for the removal of heavy metal ions and is considered to be easy to operate and cost-effective[10,11]. Up-to-date there are a number of adsorbents used for the removal of heavy metal ions, and hence synthesis of novel adsorbents is of great interest in water treatment technology.

Graphene is one of the promising material, with a two-dimensional structure and having high surface to volume ratio. Functionalized graphene has been used in the past for the adsorption of lead and cadmium ions [12,13]. Though graphene is a good adsorbent for removing the metal ions, the difficulty is to recovery of graphene adsorbent from water sample is a main

drawback. To overcome this issue, the use of magnetic nanoparticles as adsorbate will solve have been probed.

Magnetic Nanoparticles, such as Fe_3O_4 nanoparticles, γ-Fe_2O_3 nanoparticles and spinel ferrites have drawn great attention due to their nanosized properties and their potential applications in targeted drug delivery [14], magnetic fluids[15]. However, magnetic nanoparticles have ability to remove the metal ions from water with low adsorption because when the magnetic nanoparticles are in the nanosize, with sever aggregation of nanoparticles. To overcome this problem, a magnetic and graphene could be made as a composite complementary with each other. Thus the development of novel sorbents, which combines the high specific surface area of graphene and magnetic nanoparticles such as spinel ferrites, leading to the effective removal of heavy metal ions from the water [16].

The present work is focused on synthesizing graphene – magnetic hybrids for removal of heavy metal ions from water using adsorption process. Among the magnetic nanoparticles, cobalt ferrite and nickel ferrite occupy an important place due to their physical properties such as high saturation magnetization and high coercivity [17]. Herein, cobalt and nickel ferrites with graphene ($CoFe_2O_4$-G and $NiFe_2O_4$-G) nanocomposites are synthesized by a simple solvothermal method. The as-synthesized materials show good adsorption

capability of heavy metal ions with an easy separation from aqueous water. The kinetic and isotherm studies with lead and cadmium adsorption onto the as-prepared materials are also investigated in detail.

EXPERIMENTAL

Chemicals

Cobalt chloride ($CoCl_2.6H_2O$), nickel chloride ($NiCl_3.6H_2O$), ferric chloride ($FeCl_3.6H_2O$), sodium acetate, polyethelene glycol, graphite powder, sodium nitrate, potassium permanganate, hydrogen peroxide (30%) were supplied by Sd-Fine chem.Ltd, Mumbai, India. All the samples were prepared from Milli-Q water.

Preparation of CoFe₂O₄-G and NiFe₂O₄-G composite

GO was synthesized from natural flake graphite by a modified Hummers method[18]. Cobalt ferrite and nickel ferrite with graphene composite were prepared by using solvothermal process as based on our earlier method[19]. The typical procedure for preparing $CoFe_2O_4$-G and $NiFe_2O_4$-G is as follows: 300 mg of GO, 1.62 g of $FeCl_3.6H_2O$, and 0.714 g of $CoCl_2.6H_2O$ and $NiCl_3.6H_2O$ were dispersed in 150 mL of ethylene glycol (EG) with ultrasonication for 2 h. Subsequently, 10.8 g of sodium acetate and 3.0 g polyethylene glycol (PEG) were added, followed by stirring for 30 min. The mixture was then transferred to a Teflon-lined stainless steel autoclave and heated at 200 °C for 10 h. The resultant black product was washed with de-ionized water and ethanol several times by centrifugation and was dried at 45 °C in a vacuum oven. The composites $CoFe_2O_4$-G and $NiFe_2O_4$-G are denoted as GCF and GNF.

RESULTS AND DISCUSSION

Structural and morphological analysis.

Fig. S1† shows the x-ray diffraction patterns of $CoFe_2O_4$-G (GCF) and $NiFe_2O_4$-G (GNF) composites. In Fig. S1a, the crystalline planes (111), (220), (311), (400), (422), (511), (440), (620) and (533) are ascribed to the diffraction peaks at 2θ values of 18.34°, 30.19°, 35.39°, 43.11°, 53.52°, 57.11°, 62.66°, 70.90° and 74.32° respectively. All most all the diffraction peaks of GCF were assigned to the spinel-type $CoFe_2O_4$ in accordance with the standard JCPDS no. 22-1086 (Fig. S1a†) [20]. Fig. S1b† shows the x-ray diffraction patterns of $NiFe_2O_4$-G composites. The diffraction peaks at 2θ values of 18.34°, 30.11°, 35.57°, 45.91°, 54.31°, 57.11°, 62.61°, 70.90°, and 74.32° can be ascribed to the crystalline planes of (111), (220), (311), (400), (422), (511), (440), (620) and (533) respectively. The red marks of (111), (200) and (220) indicate the peaks of pure nickel phase. It can be seen that almost all the diffraction peaks of GNF were assigned to the spinel-type of $NiFe_2O_4$ in accordance with the standard JCPDS no. 86-2267 (Fig. S1b†) [21]. After the reduction of GO to graphene by solvothermal process, the reduced GO sheets were exfoliated and decorated by the $CoFe_2O_4$ and $NiFe_2O_4$ nanoparticles. This process might have led to the disappearance of the diffraction peaks of graphene (002) in accordance with the earlier reports [22]. These samples show spinel structure having Oh_7-Fd_3m space group.

The surface morphology and particle size of the as-prepared ferrite samples were further analyzed by FE-SEM and TEM. From the FE-SEM images as shown in Fig. 1, it was observed that the $CoFe_2O_4$ and $NiFe_2O_4$ nanoparticles were distributed as homogeneous spherical particles on graphene sheets. Though the particles were homogenous with the estimated cluster size ranging between 140-160 nm, they were aggregated as seen from the FE-SEM images. Structure of the GCF and GNF composites were further investigated by TEM (Fig. S2†). Porous structures are seen in both GCF (Fig S2(a,b) †) and GNF (Fig S2(c,d) †) but not in graphene. This could be clearly seen from the TEM images of GCF and GNF given in Fig. S2†. As seen from the image, the $CoFe_2O_4$ and $NiFe_2O_4$ nanoparticles were actually the aggregation of a great number of smaller nanoparticles with an average size of 10-15 nm and exhibits porous structure. $CoFe_2O_4$ and $NiFe_2O_4$ spheres were decorated on flake like graphene nanosheets with an average diameter of 150 nm. Hence it could be confirmed from the above analysis that the solvothermal route offered a homogeneous synthesis of the nanocomposites.
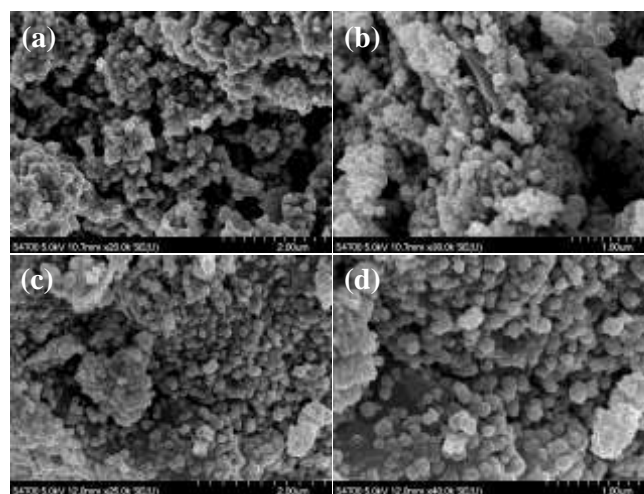
Fig. 1. FE-SEM images of (a,b) $CoFe_2O_4$-G and (c,d) $NiFe_2O_4$-G at various magnifications

In view of exploring the chemical composition of the composite, XPS measurements were recorded. The binding energy obtained in the XPS analysis was corrected for specimen charging by referencing the C 1s peak to 284.6 eV. (Distinct peaks due to C 1s, O 1s, Co 2p, Ni 3p and Fe 2p are evident in the wide scan XPS survey of GCF and GNF (Fig. 2)). The peaks obtained at 284.6, 528, 781, 68 and 710 eV correspond to the C 1s in sp2 carbon, O1s of adsorbed oxygen, Co 2p, Ni 3p and Fe 2p species respectively for both GCF and GNF. Fig. S3† and Fig. S4† shows the deconvoluted spectrum of element peaks in the composite. In the deconvoluted spectrum C 1s spectrum of GCF, four Gaussian peaks were centered at 284.6, 285.7, 286.8 and 287.5 eV. The binding energy at 284.6 and 285.7 eV could be assigned to the C-C bond (sp^2) of graphene and the C-OH respectively. Peak at 286.8 eV is ascribed to the C-O bond, while the other peak at 287.5 eV is assigned to the C=O bond [23-25]. The O1s spectra can be fitted into three peaks; (Fig. S3b†) the peak at 530.1 is characteristic of the lattice oxide oxygen of the metal oxides as Fe-O and Co-O of $CoFe_2O_4$ and the other peaks at 531.4 and 533.1 eV originates from surface adsorbed oxygen containing

species (possibly metal-OH or water molecules) due to contact with air or organic compounds such as ethylene glycol adsorbed on the surface [26,27]. In Fig. S3c, three peaks at 709.6, 710.7 and 712.1 eV are attributed to the Fe $2p_{3/2}$ and Fe $2p_{1/2}$ of Fe^{3+}, which is in agreement with $CoFe_2O_4$ [28].
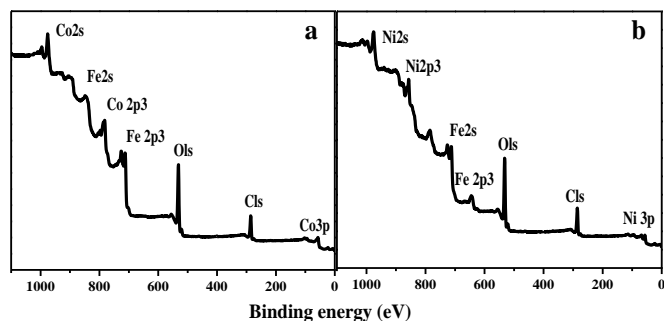
Fig. 2. XPS full Spectrum of as-prepared materials (a) $CoFe_2O_4$-G and (b) $NiFe_2O_4$-G

Two strong peaks at 780.8 and 784.9 eV for Co $2p_{3/2}$ and Co $2p_{1/2}$ were observed (Fig. S3d†), indicating the oxidation state of Co^{2+} in $CoFe_2O_4$ [28]. At the same time in the deconvoluted spectrum C 1s spectrum of GNF, four Gaussian peaks were centered at 284.6, 285.9 and 286.8 eV. The binding energy at 284.6 and 285.9 eV could be assigned to the C-C bond (sp^2) of graphene and the C-OH respectively. Peak at 286.8 eV is ascribed to the C-O bond. The O1s spectra can be fitted into four peaks; (Fig. S4b) the peak at 529.6 and 529.9 is characteristic of the lattice oxide oxygen of the metal oxides as Fe-O and Co-O of $NiFe_2O_4$ and the other peaks at 531.1 and 532.8 eV originates from surface adsorbed oxygen containing species (possibly metal-OH or water molecules) due to contact with air or organic compounds such as ethylene glycol adsorbed on the surface. In Fig. S4c†, three peaks at 709.5, 710.4 and 712.8 eV are attributed to the Fe $2p_{3/2}$ and Fe $2p_{1/2}$ of Fe^{3+}, which is in agreement with $NiFe_2O_4$. [29] Two strong peaks at 67.4 and 68.49 eV for Ni $3p_{3/2}$ and Ni $3p_{1/2}$ were observed (Fig. S4d†), indicating the oxidation state of Ni^{2+} in $NiFe_2O_4$ [29].

Excellent magnetic performance is necessary for a material to be a good magnetic adsorbent. Field dependent magnetization of the synthesized composite was measured at 27°C at an applied field of $-10,000 \leq H \leq 10,000$ Oe. Fig. 3 shows the magnetic hysteresis loop of the as-prepared GCF and GNF in the presence and absence of graphene, which indicates their super paramagnetic nature. A saturation magnetization of 32.79 and 49.55 emu/g was observed for $CoFe_2O_4$-G (GCF) and bare $CoFe_2O_4$ respectively and for $NiFe_2O_4$-G (GNF) and bare $NiFe_2O_4$ was observed as 24.28 and 36.10 emu/g respectively. As compared to bare $CoFe_2O_4$ and $NiFe_2O_4$, the saturation magnetization decreases due to the contribution of graphene layers [30]. As previously observed from FE-SEM and TEM images, $CoFe_2O_4$ and $NiFe_2O_4$ particles were homogenously decorated on the graphene layers, which act as magnetically inactive layers in turn affecting the magnetization [31]. The remanant magnetization (Mr), a measure of the remaining magnetization when the driving field is dropped to zero are 5.186 and 0.988 emu/g for $CoFe_2O_4$ and $CoFe_2O_4$-G respectively and for $NiFe_2O_4$ and $NiFe_2O_4$-G 1.426 and 0.681 emu/g respectively. Thus GCF and GNF with high saturation magnetization values can quickly respond to the external

magnetic field, which is beneficial to their application in high capacity adsorption. Hence, such materials could be used as a reusable adsorbent for fast, convenient and highly efficient removal of heavy metal ions from water samples.
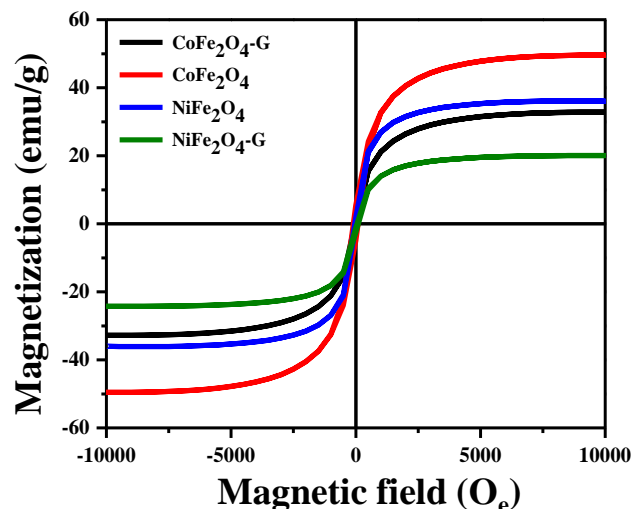
Fig. 3. Hysteresis loops of $CoFe_2O_4$ and $NiFe_2O_4$ nanoparticles in the presence and absence of graphene at 300 K

To determine the porous capacity of GCF and GNF for the uptake of gases, N_2 adsorption–desorption isotherm was measured and as shown in Fig. 4. The N_2 gas adsorption–desorption isotherm displays type IV curve and H3 hysteresis loop according to IUPAC (International Union of Pure and Applied Chemistry) classification. This behaviour shows the predominance of mesopores [32,33]. Type H3 hysteresis indicates the random distribution of pores and also the interconnection of pores. These properties of pores, significantly control desorption isotherm than adsorption isotherm because adsorption and desorption isotherm show a different behaviour with effect to pore network at a relative pressure of 0.45 (for N_2 at 77 K). BET surface area measurement and t-plot analysis were carried out for knowing the specific surface area of the as-prepared material. The BET surface area plot of GCF and GNF composite (Fig.4b) corresponds to the BET equation [34]. The specific surface area of GCF and GNF was found to be 126.36 and 57.11 m^2/g, using the Brunauer-Emmett-Teller (BET) method. The plot between the volumes of nitrogen adsorbed (Q) for different P/P0 values as a function of thickness of adsorbed gas, t for GCF and GNF composites is given in Fig. 4c. The Barrett-Joyner-Halenda (BJH) desorption average pore diameter was 3.6 nm with a very wide pore size distribution, and the corresponding single-point total pore volume at P/P0 = 0.995 is 0.206 cm^3/g (Fig. 4d). The experimental point of this t-plot is in agreement with the Harkins and Jura isotherm equation [35]. It is clearly evident from the plot that experimental data points fall in a straight line for t = 0.36-0.49 nm (linear portion of the curve). Thus, the GCF and GNF are porous in nature, as t-plot was not passing through the origin. Fitted linear line showed positive intercept, which confirmed the presence of mesopores in GCF and GNF nanocomposites [19].

Adsorption Parameters
To explore the adsorption behaviour of the composite, batch mode adsorption was carried out as explained in the previous
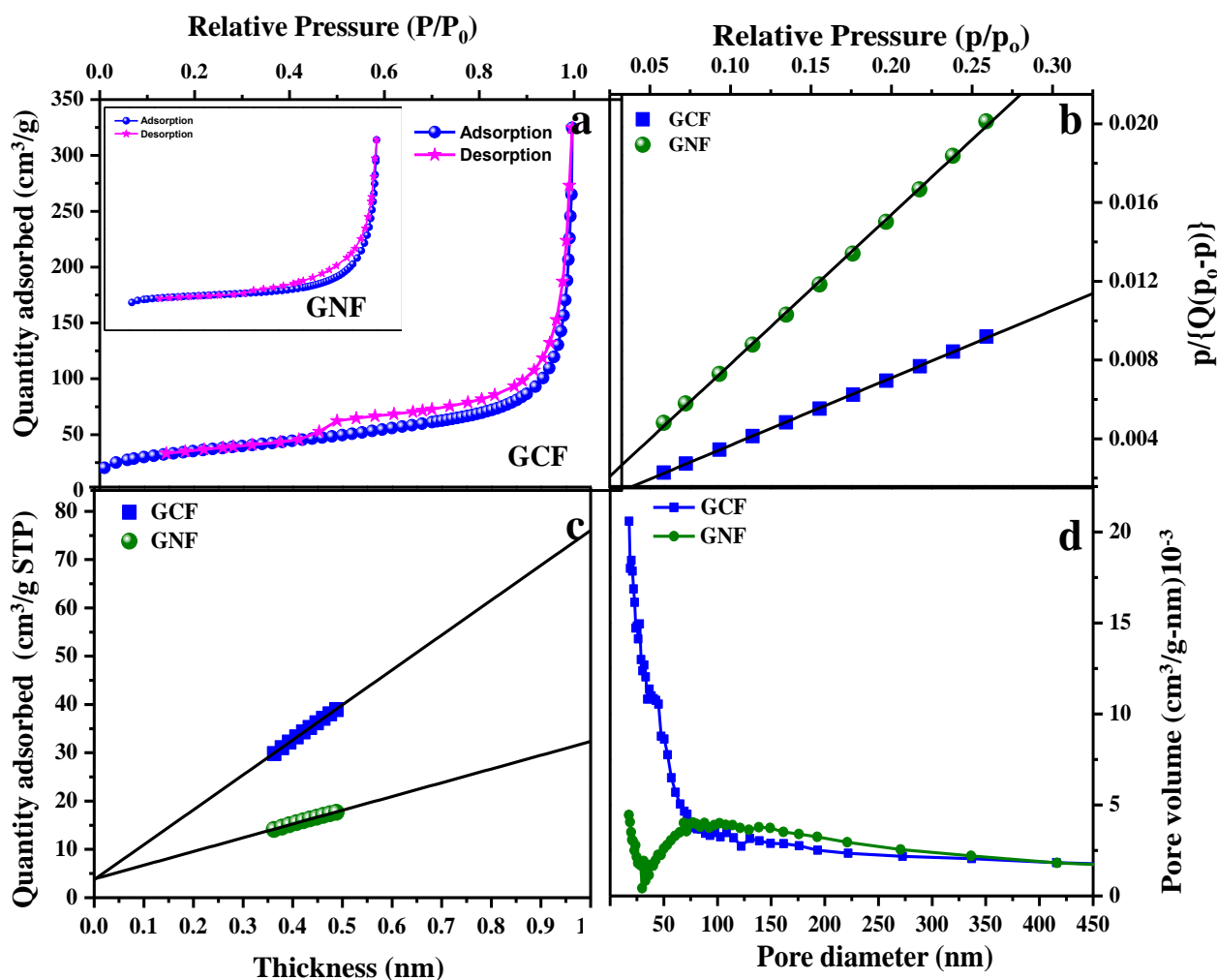
Fig. 4. (a) N_2 adsorption - desorption isotherms of GCF (inset shows GNF) (b) BET surface area (c) t-plot analysis and (d)Pore size distribution of both GCF and GNF nanocomposites.

section. The adsorption percentage and loading capacity of metal ions were calculated as follows:

$$Adsorption \text{ (\%)} = \frac{C_i - C_f}{C_i} \times 100 \quad (1)$$

$$q_e = \frac{v(C_i - C_e)}{W} \quad (2)$$

where C_i and C_f being the initial and final metal ion concentration; q_e and C_e are equilibrium adsorption capacity and concentration of the metal ions at equilibrium; v is the volume of metal ion solution (L) and W is the weight of adsorbent in grams.

Contact time measurements depict the possible rapidness of binding and removal of metal ions by the adsorbent and optimum time for the removal of heavy metal ions. The adsorption of Pb and Cd on GCF and GNF at T = 37°C, Ci = 20 mg/L and adsorbent dosage = 25 mg/L were carried out in order to optimize the contact time of the ions with the adsorbent. Fig. 5a shows the percentage of adsorbed Pb^{2+} and Cd^{2+} ions onto GCF and GNF surface, as a function of contact time. It should

be noted that the adsorption of Pb^{2+} and Cd^{2+} increased quickly with time and then reached equilibrium. The adsorption is quick due to the availability of plenty vacant surface active sites on the adsorbent surface at an initial stage. Moreover, as the duration increased, it was observed that the available active sites are unavailable resulting in decrease in driving force, lengthening of the equilibrium level and hence slowing down the adsorption rate. Fig. 5a clearly shows that, it took about 100 min to reach adsorption equilibrium for Pb and Cd ions onto GCF and 180 min for Pb and Cd ions onto GNF respectively. Therefore 100 min was kept as optimized time for Pb and Cd ions adsorption onto GCF and 180 min for Pb and Cd ions adsorption onto GNF for all further parameter studies.

The adsorption property of the as-prepared material was analyzed with an effect of pH as it has a direct influence on the adsorption property. The initial concentrations of both metal ions were 20 mg/L at 37°C. The pH values were varied from 2 to 8 for both Pb and Cd ions, at the same concentrations of metal ions. Fig. 5b depicts that the adsorption increased with pH in acidic condition, which then reached a maximum at pH 7.0. It is thus concluded that GCF and GNF surfaces have maximum removal efficiency at pH 5 and 7 for Pb and Cd ions respectively.
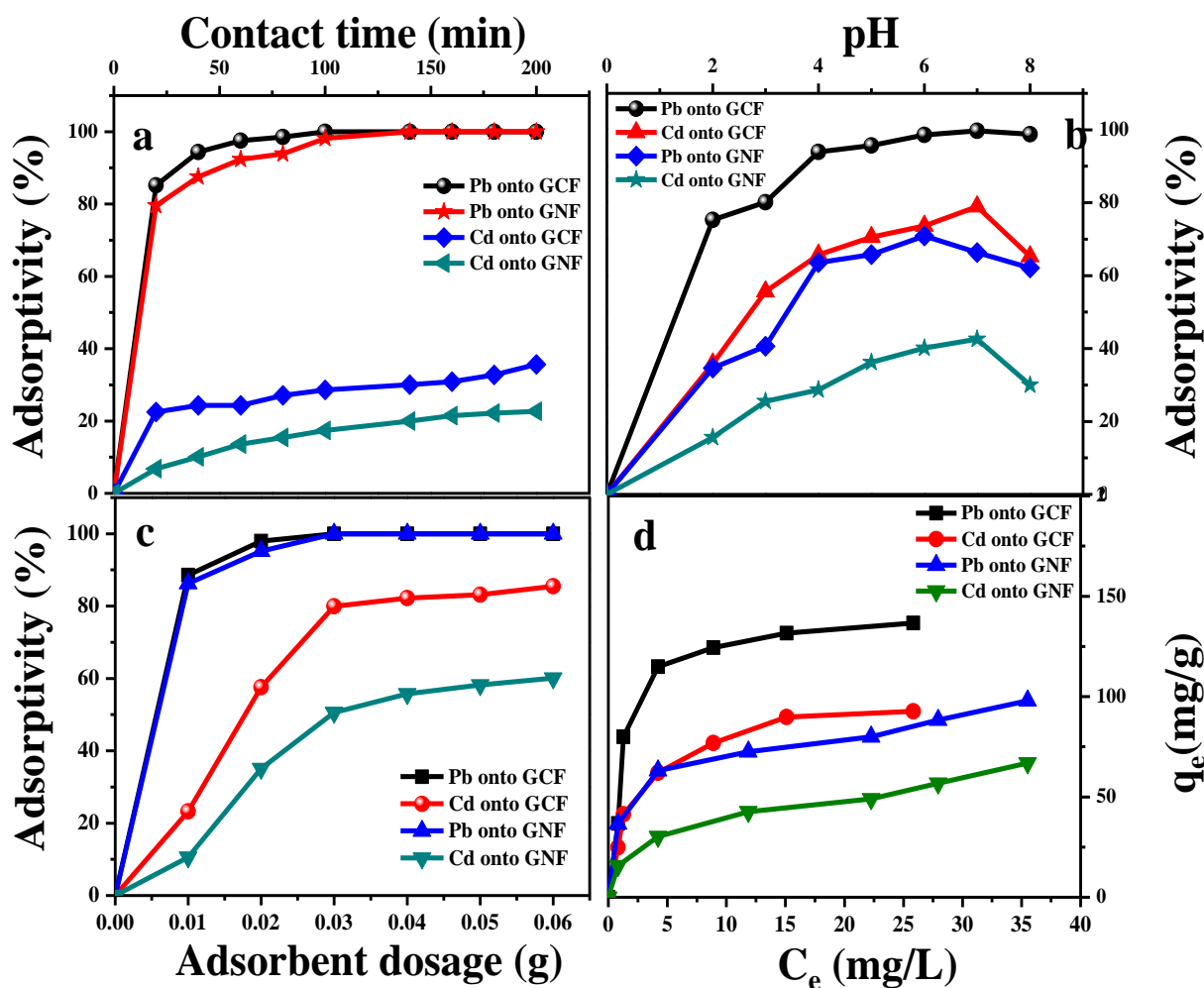
Fig. 5. Effect of (a) contact time (b) pH (c) adsorbent dosage and (d) adsorption isotherm on percentage of lead and cadmium ions adsorption onto GCF and GNF respectively, initial conc. 20 mg/L, T = 37°C.

While conducting batch mode studies, adsorbent dosage is one of the important parameters. The effect of adsorbent dosage on the removal of Pb^{2+} and Cd^{2+} ions were studied by varying dosage concentration from 0.01 to 0.07 g/L. The adsorption capacities of both the ions increased with an increase of adsorbent dosage, due to the large number of active sites on the adsorbent surface available for adsorption and hence removal of metal ion efficiency was increased. As all the active sites may not be available for adsorption, it leads to saturation. The point of saturation for Pb^{2+} ions were found at 0.03 g/L for GCF with 100% removal efficiency and for Cd^{2+} ions 0.03 g/L with an removal efficiency of 80%, whereas for GNF 0.03 g/L for Pb ions with an efficiency of 100% and 0.05 g/L for Cd ions with an 50% of removal efficiency respectively as shown in Fig. 5c. Fig. 5d shows the adsorption isotherm of Pb and Cd ions onto GCF and GNF surface at pH 5 and 7. Seven different initial concentrations of Pb and Cd ions were taken in the range of 10-70 mg/L at 37°C. The adsorption percentage increased with an increase of Ce and a maximum sorption of 140 and 100 mg/L was obtained for Pb ions onto GCF and GNF respectively, whereas for Cd ions maximum sorption capacity

of 100 and 75 mg/L was obtained onto GCF and GNF respectively.

Two isotherm models were studied for adsorption equilibrium, one is Langmuir isotherm model and another is Freundlich isotherms. Regression coefficient (R^2) is the factor which validates the isotherm model. If the adsorption was predicted as monolayer, it follows Langmuir adsorption isotherm with a finite number of identical sites onto the surface of adsorbent. Langmuir adsorption model [36], follows the below equation:

$$\frac{c_e}{q_e} = \frac{1}{k_d q_m} + \frac{1}{q_m} C_e \qquad (3)$$

Where C_e (mg/L) is the equilibrium concentration of metal ions, q_e and q_m (mg/g) are the adsorption capacity at equilibrium and maximum adsorption respectively, and K_d (L/mg) is the affinity binding constant.

The values of q_m and K_d were obtained from intercept and slope of the linear plot of C_e/q_e against C_e. If the adsorption is multi-layer, it follows Freundlich isotherm model with a heterogeneous surface onto the adsorbent. The following expression allows Freundlich isotherm model [37].

$$\ln q_e = \ln k_f + \frac{1}{n}\ln C_e \qquad (4)$$

While K_f and n are physical constants representing the adsorption capacity and intensity of adsorption, respectively.

The parameter which varies the isotherm models are listed in Table S1†. Regression coefficient (R^2) values of Langmuir isotherms are 0.993 and 0.989 for Pb ions onto GCF and GNF, whereas for Cd ions 0.997 and 0.964 onto GCF and GNF respectively. For Freundlich isotherms are 0.862 and 0.926 for Pb ions onto GCF and GNF, whereas for Cd ions 0.985 and 0.958 onto GCF and GNF respectively (Fig. S5). These results show that the Langmuir isotherm model suited well for adsorption of both the metal ions onto GCF and GNF and hence the adsorption is monolayer type. In addition to this, a maximum adsorption capacity q_m (mg/g) of Pb ions onto GCF and GNF was calculated to be 142.85 and 111.11 mg/g respectively, whereas for Cd ions it is calculated as 105.26 and 74.62 mg/g with GCF and GNF adsorbents respectively.

Adsorption Kinetic studies

The adsorption kinetics of metal ions with GCF and GNF was investigated by two kinetic models, Lagergren pseudo-first-order and pseudo-second-order models.

The theoretical q_e values of both heavy metal ions were closer to the calculated experimental values and the correlation coefficient (R^2) for the pseudo-second-order kinetic model for the adsorption of Pb and Cd ions onto GCF and GNF nanocomposites is 0.999, 0.998 and 0.998, 0.989 and that of pseudo-first-order kinetic model is 0.975, 0.966 and 0.958,0.945 respectively.
The results show that pseudo-second-order kinetic model provides a better correlation as compared to pseudo-first-order kinetic model for the adsorption of Pb and Cd ions onto GCF and GNF nanocomposites.

Thermodynamic parameters

The values of enthalpy change ($\Delta H°$) and entropy change ($\Delta S°$) were calculated from slope and the intercept of the plot of $\ln K_o$ vs $1/T$
Gibb's free energy $\Delta G°$ is given by

$$\Delta G^0 = -RT\ln k_0 \qquad (5)$$

where R is the gas constant, T is the absolute temperature and K_0 is thermodynamic equilibrium constant related to Langmuir constant K_d.

$$\ln k_0 = -(\frac{\Delta H^0}{R}\frac{1}{T} + \frac{\Delta S^0}{R}) \qquad (6)$$

The free energy change is determined from equation 5 and 6 and the calculated thermodynamic parameters (extracted from slope and intercept of $\ln K_o$ vs $1/T$) are tabulated in Table 1 and 2 for GCF and GNF respectively.

A negative standard enthalpy change suggests that the interaction of Pb and Cd ions onto GCF and GNF is exothermic, which is supported by the increasing adsorption of Pb and Cd ions with an increase in temperature. A negative value of Gibb's free energy confirms that the adsorption is spontaneous, which becomes more negative with an increase in temperature. This indicates that a higher adsorption has actually occurred at higher temperatures [38].

Table 1: Adsorption thermodynamic parameters for the percentage of ion adsorption onto GCF nanocomposite

Metal ions	Temp (K)	$\Delta G°$ (kJmol^{-1})	$\Delta H°$ (kJmol^{-1})	$\Delta S°$ (Jmol^{-1}k^{-1})
Pb(II)	300	-9.58		
	310	-10.46	-5.40	14.88
	320	-9.82		
Cd(II)	300	-1.52		
	310	-1.89	-3.94	2.64
	320	-3.90		

Table 2: Adsorption thermodynamic parameters for the percentage of ion adsorption onto GNF nanocomposite

Metal ions	Temp (K)	$\Delta G°$ (kJmol^{-1})	$\Delta H°$ (kJmol^{-1})	$\Delta S°$ (Jmol^{-1}k^{-1})
Pb(II)	300	-7.88		
	310	-9.06	-4.15	13.65
	320	-8.14		
Cd(II)	300	-1.97		
	310	-1.98	-13.34	25.31
	320	-1.70		

Desorption and regeneration studies

Desorption and regeneration studies of the as-prepared nanocomposites are of crucial importance when assessing for commercial applications. The adsorption of metal ions was done as explained in batch mode adsorption section. For desorption, metal loaded $CoFe_2O_4$-G and $NiFe_2O_4$-G (0.025 g) was shaken with 50 ml of 0.01 M HCl as the desorbing agent at 250 rpm for 2 hrs at 37°C. The adsorbent was separated by centrifugation and the supernatant was filtered with 0.22 µm cellulose nitrate membranes. The obtained filtrate was analyzed for metal ion detection using AAS analysis and the metal desorbed $CoFe_2O_4$-G and $NiFe_2O_4$-G were used as a regenerated adsorbent. The adsorption-desorption was repeated for three cycles to determine the reusability potential of the adsorbent. It was found that for both materials, desorbing capacity of metal ions were 100% to 98% for three cycles as shown in Fig. S6 for both the metal ions. The efficiency was almost retained during three repeated cycles. The above experiments indicated that the adsorbents could be regenerated for practical use.

CONCLUSIONS

A novel ferrite based composite GCF and GNF were synthesized successfully by solvothermal process and further tested for adsorption of heavy metal ions viz. Pb and Cd ions from aqueous water. The as-synthesized materials were having large surface area which was observed from the BET surface area analysis. Adsorption of Pb and Cd ions onto to the as-prepared materials GCF and GNF surfaces follows that the experimental data analysis were well fitted to the Langmuir

isotherm model. The monolayer adsorption capacity of both heavy metals; Pb and Cd onto GCF and GNF were found to be the highest adsorption equilibrium for Pb(II) is 142.8 and 111.1 mg/g at pH of 5 and 310 K for $CoFe_2O_4$-G& $NiFe_2O_4$-G; while for Cd(II) was 105.26 and 74.62 mg/g at pH of 7 and 310 K.. Thermodynamic properties signifies that the adsorption reaction was spontaneous and exothermic. Hence, the prepared composite could be used as an absorbent for the removal of heavy metal ions for environmental applications.

Acknowledgements

Notes and references

[a] Center for Nanotechnology Research, VIT University, Vellore, India, 632014.

[b] Thin Film Magnetism group, Cavendish Laboratory, Department of Physics, University of Cambridge, Cambridge CB3 OHE, UK.

[c] Climate Change Technology Research Division, Korea Institute of Energy Research, Yuseong-gu, Daejeon 305-343, South Korea.

† Electronic Supplementary Information (ESI) available: Supplementary data includes characterization tools, Figures and Tables.
See DOI: 10.1039/b000000x/

References

1   Z.J. Liu, L. Chen, Z.C. Zhang, Y.Y. Li, Y.H. Dong and Y.B. Sun, J. Mol. Liq. 2013, **179**, 46–53.

2   S.B. Deng and Y.P. Ting, Langmuir 2005, **21,** 5940–5948.

3   D.D. Shao, C.L. Chen and X.K. Wang, Chem. Eng. J. 2012, **185–186**, 144–150.

4   J.N. Armor, Appl. Catal. B-Environ. 1992, **1**, 221–256.

5   P. Biswas and C.Y. Wu, J. Air Waste Manage. Assoc. 1998, **48**, 113–127.

6   D. Zhang, S. Wei, C. Kaila, X. Su, J. Wu, A. B. Karki, D. P. Young and Z. H. Guo, Nanoscale., 2010, **2**, 917-919.

7   C. Kennes, E.R. Rene and M.C. Veiga, J. Chem. Technol. Biotechnol. 2009, **84**, 1419–1436.

8   M.C. Delhomenie and M. Heitz, Crit. Rev. Biotechnol. 2005, **25**, 53–72.

9   G.M. Gadd, J. Chem. Technol. Biotechnol. 2009, **84**, 13–28.

10 S.P. Dubey, K. Gopal and J.L. Bersillon, J. Environ. Biol. 2009, **30**, 327–332.

11 S. Wang and Y. Peng, Chem. Eng. J. 2010, **156**, 11–24.

12 X.J. Deng, L.L. Lü, H.W. Li and F. Luo, J. Hazard. Mater. 2010, **183**, 923–930.

13 G.X. Zhao, X.M. Ren, X. Gao, X.L. Tan, J.X. Li, C.L. Chen, Y.Y. Huang and X.K.Wang, Dalton Trans. 2011, **40**, 10945–10952.

14 X.Y. Yang, X.Y. Zhang, Y.F.Ma, Y. Huang, Y.S. Wang and Y.S. Chen, J. Mater. Chem. 2009, **19**, 2710-2714.

15 N. Wang, L. Zhu, D. Wang, M. Wang, Z. Lin and H. Tang, Ultrason. Sonochem., 2010, **17**, 526-533.

16 C. Santhosh, P. Kollu, S. Doshi, M. Sharma, D. Bahadur, M.T. Vanchinathan, P. Saravanan, B. S. Kim and A. Nirmala Grace, RSC Adv. 2014, **4**, 28300

17 H. Zheng, J.Wang, S.E. Lofland, Z. Mohaddes-Ardabili, L. Ma, T. Zhao, L. Salamanca-Riba, S.R.Shinde, S.B. Ogale, F. Bai, D. Viehaland, Y. Jia, D.G. Schlom, M. Wuttig, A. Roytburd and R.Ramesh, Science 2004, **303**, 661.

18 W.S. Hummers and R.E. Offeman, J. Am. Chem. Soc. 1958, **80**, 1339-1339.

19 S. Chella, P. Kollu, E. V. P. R. Komarala, S. Doshi, M. Saranya, S. Felix, R. Ramachandran, P. Saravanan, V. L. Koneru, V. Venugopal,S. K. Jeong and A. Nirmala Grace, Appl. Surf. Sci. 2015, **327**, 27–36.

20 N.W. Li, M.B. Zheng, X.F. Chang, G.B. Ji, H.L. Lu, L.P. Xue, L.J. Pan and J.M. Cao, J. Solid. State Chem 2011, **184**, 953-958.

21 P. Kollu, S. Prathapani, E.K. Varaprasadrao, C. Santosh, S. Mallick, A.Nirmala Grace and D. Bahadur, Appl.Phy.Lett. 2014, **105**, 052412.

22 Y.S. Fu and X. Wang, Ind. Eng. Chem.Res. 2011, **50**, 7210–7218.

23 V. Chandra, J. Park, Y. Chun, J.W. Lee, I.C. Hwang and K.S. Kim, ACS Nano 2010, **4**, 3979-3986.

24 X.L. Wu, L. Wang, C.L. Chen, A.W. Xu and X.K. Wang, J. Mater. Chem. 2011, **21**, 17353–17359.

25 Z.J. Fan, W. Kai, J. Yan, T. Wei, L.J. Zhi, J. Feng, Y.M. Ren, L.P. Song and F. Wei, ACS Nano 2011, **5**, 191–198.

26 W. Xia, X. Chen, S. Kundu, X. Wang, G. Grundmeier, Y. Wang, M. Bron, W. Schuhmann and M. Muhler, Surf. Coat. Technol. 2007, **201**, 9232–9237.

27 C.R. Brundle, T.J. Chuang and K. Wandelt, Surf. Sci. 1997, **68**, 459–468.

28 Y. Fu, H. Chen, X. Sun and X. Wang, Appl. Catal. B Envi. 2012, **111–112**, 280–287.

29 L. Chen, H. Dai, Y. Shen and J. Bai, J. Alloys. Comp. 2010, **491**, L33-L38.

30 H. Deng, X.L. Li, Q. Peng, X. Wang, J.P. Chen and Y.D. Li, Angew. Chem. Int. Ed. 2005, **44**, 2782–2785.

31 S. Rana, J. Rawat and R.D.K. Misra, Acta Biomater. 2005, **1**, 691–703.

32 K.C. Barick, S. Sarika, M. Aslam and D. Bahadur, Micropor. Mesopor. Mater. 2010, **134**, 195–202.

33 K.S.W. Sing, D.H. Everett, R.A.W. Haul, L. Moscou, R.A. Pierotti, J. Rouquerol and T. Siemieniewska, Pure Appl. Chem. 1985, **57**, 603-619.

34 J.C. Groen, L.A. Peffer and J. Perez-Rremirez, Micropor. Mesopor.Mater. 2003, **60**, 1-17.

35 W.D. Harkins and G. Jura, Surface of solids XIII, J. Am. Chem. Soc. 1944, **66**, 1366-1372.

36 B. Kizilkaya and A.A. Tekinay, Sci. Adv. Mater. 2011, **3**, 949-961.

37 S.T.Yang, Y. Chang, H. Wang, G. Liu, S. Chen, Y. Wang, Y. Liu and A. Cao, J. Colloid Interface Sci. 2011, **351**, 122–127.

RSC Advances Accepted Manuscript

38   O. Yavuz, Y. Altunkaynak and F. Guzel, Water. Res. 2003, **37**, 948-952.